Apparatus for the room temperature measurement of low field Nernst and magneto-Seebeck coefficients

Cite as: Rev. Sci. Instrum. 95, 083903 (2024); doi: 10.1063/5.0222406

Submitted: 7 June 2024 • Accepted: 29 July 2024 •

Published Online: 14 August 2024











C. E. Porter, 1,a) C. M. Crawford, 2 and E. S. Toberer 1



AFFILIATIONS

- ¹ Materials Science, Colorado School of Mines, Golden, Colorado 80401, USA
- ²Jet Propulsion Laboratory, California Institute of Technology, Pasadena, California 91011, USA
- ^{a)}Author to whom correspondence should be addressed: c7porter@gmail.com

ABSTRACT

Nernst coefficient measurements are a classic approach to investigate charge carrier scattering in both metals and semiconductors. However, such measurements are not commonly performed, despite the potential to inform material design strategies in applications such as thermoelectricity. As dedicated instruments are extremely scarce, we present here a room temperature apparatus to measure the low field Nernst coefficient (and magneto-Seebeck coefficient) in bulk polycrystalline samples. This apparatus is specifically designed to promote accurate and facile use, with the expectation that such an instrument will make Nernst measurements de rigueur. In this apparatus, sample loading and electrical contacts are all pressure-based and alignment is automatic. Extremely stable thermal control (10 mK of fluctuation when $\Delta T = 1$ K) is achieved from actively cooled thermoelectric modules that operate as heaters or Peltier coolers. Magneto-Seebeck measurements are integrated into the system to correct for residual probe offsets. Data from the apparatus are provided on bulk polycrystalline samples of bismuth, InSb, and SnTe, including raw data to illustrate the process of calculating the Nernst coefficient. Finally, we review how Nernst measurements, in concert with Seebeck, Hall, and electrical resistivity, can be analyzed via the Boltzmann equation in the relaxation time approximation to self-consistently predict the Fermi level, effective mass, and energy-dependent relaxation time.

Published under an exclusive license by AIP Publishing. https://doi.org/10.1063/5.0222406

I. INTRODUCTION

The Nernst effect is the induced transverse electric field E_{ν} in response to a longitudinal temperature gradient $\nabla_x T$ and an applied magnetic field B_z [Fig. 1(a)]. Analogous to the Hall effect, where the electric field is $E_{Hall} = R_H(J \times B)$, the Nernst electric field is defined as

$$\mathbf{E}_{Nernst} = N\mathbf{B} \times \nabla T. \tag{1}$$

Here, N is the Nernst coefficient, which is typically on the order of nV/KT to μ V/KT for most conductive materials. ⁴⁻⁶ Nernst measurements have an impressive history of providing insight into the energy dependence of charge carrier transport in materials ranging from semimetals to classic thermoelectrics to superconductors. In particular, Nernst measurements have resolved the energy dependence of charge carrier scattering and, thus, the dominant scattering mechanisms.3

The Nernst effect resembles the Hall effect in that both measurements utilize the Lorentz force to generate a transverse voltage in a magnetic field. These two measurements provide unique insights into material properties due to their distinct origins. This is a result of the current in the Hall effect being electrically driven (df/dE) vs thermally driven in the Nernst effect (df/dT). In the Hall effect, the charge carriers that contribute most to the induced voltage reside at the Fermi level (E_F) . The charge carriers participating in the Nernst effect are those residing slightly above and slightly below E_F . On the shown in Fig. 1(b), df/dT = 0 at E_F ; hence, carriers with energy equal to E_F do not contribute to this particular effect.

The Nernst effect also has similarities to the Seebeck effect, in that an applied temperature gradient drives a thermal current of holes and electrons. As such, both measurements probe the same population of carriers, namely, those residing slightly above and below the Fermi level [Fig. 1(b)]. 10,111 However, the longitudinal See-

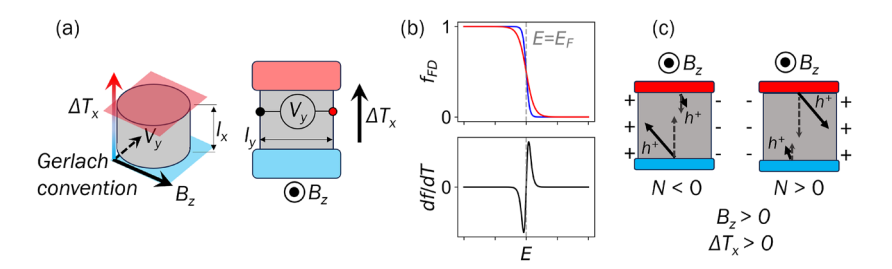


FIG. 1. (a) The sample geometry for our Nernst measurements involves a cylindrical sample. The temperature gradient is applied along the *x*-axis, the magnetic field is applied along the *z*-axis, and the transverse Nernst voltage V_y is measured. The side view of the sample is shown to clearly indicate the location of the voltage probes. We adopt the historical Gerlach sign convention (in which the Nernst signal of bismuth is negative). (b) Top panel: The Fermi–Dirac distribution is shown at two temperatures; here, the higher temperature is red (see online for color) and the lower temperature is blue. At the Fermi level $(E = E_F)$, the two distributions intersect. Bottom panel: The temperature derivative of the Fermi–Dirac distribution (df/dT) is the function that drives the carrier diffusion responsible for the Seebeck and Nernst effect [Eq. (16)]. Carriers with energy close but not equal to E_F contribute the most to these thermoelectric effects. (c) The induced Nernst voltage is the result of charge carriers with different energies being preferentially scattered. Those with a shorter relaxation time are more rapidly scattered away; those with a longer time are more strongly deflected by the Lorentz force. The left panel reflects a regime where lower energy carriers (closer to the band edge) have a longer relaxation time, as in acoustic phonon scattering. This leads to a negative Nernst signal. The right panel shows the case of a positive Nernst coefficient, where higher energy carriers have a longer relaxation time, as in ionized impurity scattering.

beck effect is an electrical field that is induced along the same axis as the applied temperature gradient, whereas the Nernst signal¹² is perpendicular to the temperature gradient.^{1,10,13} Furthermore, Seebeck coefficient measurements are generally sample geometry-independent, whereas Nernst measurements are sensitive to the sample geometry. Rearranging Eq. (1) for the measured transverse Nernst voltage and adopting the coordinate scheme in Fig. 1(a),

$$V_y = N\Delta T_x B_z \frac{l_y}{l_x}. (2)$$

We see that the sample geometry (l_y/l_x) has a significant impact on the magnitude of the measured voltage.

Nernst measurements yield information beyond what is offered by electrical resistivity, Hall effect, and Seebeck coefficient measurements. These traditional measurements provide information about the majority carrier type, carrier concentration, and Fermi level position. The Nernst coefficient is incredibly sensitive to scattering, and the polarity of the coefficient yields information on the dominant scattering mechanism. 7,13-15 This is in contrast with the Hall and Seebeck coefficients, whose polarity typically reflects the polarity of the primary charged carrier type. Within the single parabolic band regime, Nernst measurements can be analyzed using the method of four coefficients to determine the dominant carrier scattering mechanism. 3,4,6,8,9 When analyzing materials where the single parabolic band approximation does not apply, Nernst measurements can be analyzed with the general Boltzmann transport equation within the relaxation time approximation, as discussed in Sec. IV.

Nernst measurements to date are frequently conducted at cryogenic temperatures to probe exotic phenomena such as superconductivity. $^{2.5,16-18}$ For conventional metals and semiconductors, the Nernst signal is also typically measured at temperatures below 300 K. $^{19-21}$ Practically, Nernst is an excellent phenomenon to measure at low T because the signal often strengthens with decreasing T. Whereas the magnitude of the Seebeck coefficient often decays

monotonically toward zero upon cooling from room temperature, the low field [$\mu B \ll 1$, μ : mobility (m²/V s), B: magnetic field (T)] Nernst coefficient is generally observed to peak between 0 K and room temperature. ^{5,18,22} This is because the electron relaxation time τ typically grows with decreasing temperature, leading to a greater buildup of carriers contributing to the Nernst voltage [Fig. 1(c)]. For example, the Nernst coefficient of bismuth increases from 0 to 100 K²²² and then decreases at higher temperatures. ^{22,23} At 100 K, the N of bismuth is $-183~\mu V/KT$, but by 300 K, it has plummeted in magnitude to $-14~\mu V/KT$. This is still a sizable signal as far as N goes, and in fact, bismuth possesses one of the largest Nernst signals known to date. ¹⁶

Cryogenic Nernst measurements are generally performed on very small, thin film or bulk samples in a measurement system such as a Quantum Design PPMS.^{8,22} The measurement typically requires the wire bonding of eight or more delicate contacts to the sample—four for reading ΔT , two for measuring V_{ν} , and at least two more for supplying heat, typically via a small resistive heater. The Nernst coefficient is derived from either (i) dV/dB at a constant ΔT or (ii) dV/dT at a constant B. Systems performing the former are more common and more accurate. 5,8 For example, Wang et al. found that method (i) yielded Nernst coefficient data accurate to 0.1 μ V/KT, and method (ii) produced less accurate data, even when the temperature was swept at a slow rate of 1 K/min. The authors attributed this loss of accuracy to the long relaxation time of the temperature gradient within the crystal.⁵ In addition, Nernst measurements performed in cryostats face challenges at room temperature regarding thermometry sensitivity and longer equilibration times since the sample temperature is much closer to the heat bath temperature.

Room temperature Nernst measurements are not nearly as commonly reported as Seebeck, Hall, or resistivity measurements. Most measurements of the Nernst coefficient above 300 K are conducted using a cryostat. ^{19,24} Furthermore, we are aware of one system designed specifically for high temperature measurements. ²⁵ We posit that this scarcity is due to two separate reasons. First,

since the Nernst signal scales with electronic mobility, 16 the induced Nernst voltage is often too small to be measured in low mobility samples, especially above room temperature when mobility is limited by acoustic phonon scattering. Second, while Hall and Seebeck effect instruments $^{26-28}$ have experienced rapid advancements in usability and accuracy [i.e., pressure contacts instead of tedious wire bonding, using the differential method (small ΔT) in lieu of the integral method (large ΔT) for measuring the Seebeck coefficient], Nernst has not experienced such a renaissance yet.

Here, we demonstrate a near-room temperature Nernst coefficient measurement system that is designed for both accuracy and usability. To maximize usability, the system was designed to be simple to load, with self-aligning pressure contacts for measuring V_y . Furthermore, the cylindrical sample geometry is compatible with other standard thermoelectric instruments and requires no specific machining of the sample. All terms in Eq. (2) were considered in the context of maximizing accuracy. Examples include (i) incorporating Peltier coolers to deliver an extremely stable ΔT , (ii) precise pressure contacts to minimize geometry uncertainty, and (iii) the incorporation of magneto-Seebeck measurements to correct for any residual probe offsets. In the following, we detail these specific design choices, provide example measurements on a variety of materials, and discuss the analysis of Nernst coefficient data.

II. INSTRUMENTATION

An apparatus to measure the low field Nernst coefficient N must supply a thermal gradient dT/dx and magnetic field B_z to the sample and measure the induced transverse voltage V_{ν} [Eq. (2)]. Our measurement setup consists of two copper heater/cooling blocks with embedded Peltier modules on either side of the sample [half of the setup shown in Fig. 2(a)], two constantan-copper (type T) thermocouples [one embedded in each copper block, one shown in Fig. 3(c)], a ring containing the two electrical contacts to measure the Nernst voltage [Fig. 3(a)], and an electromagnet to achieve +/-1 T. Each of these hardware components interfaces with a computer via Python [Fig. 4(b)]. Python is used to write settings to and read data from each hardware component, improving the ease of data collection as well as minimizing the chance of human error in calculating the Nernst coefficient. Given that the Nernst signal rarely exceeds a few μV , 5,29 careful instrumentation design is required to achieve high sensitivity and minimize uncertainty. In the following sections, we describe our design to minimize the uncertainty that each hardware component introduces to the calculation of the Nernst coefficient.

A. Thermal control

Our thermal design criteria are (i) ability to apply a stable ΔT of at least 1 K in a temperature regime near or below room temperature without a cryostat, (ii) achieving excellent thermal contact between the sample and sample holder such that heat flow is only along one dimension, and (iii) accurately controlling and measuring the temperature of each block.

1. Heating/cooling blocks

Our thermoelectric setup operates between 0 and $40\,^{\circ}\text{C}$ with mirrored Peltier coolers. The sample is clamped between two

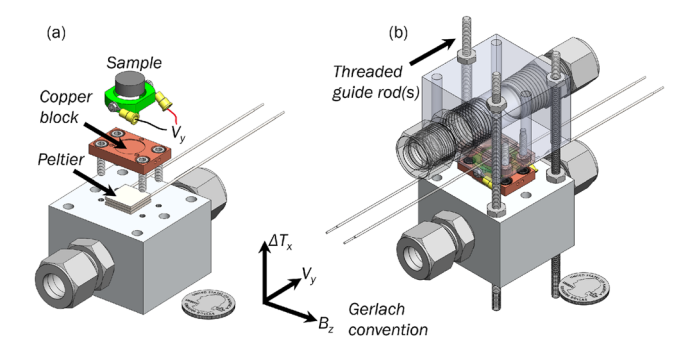


FIG. 2. (a) This schematic shows the lower half of the stage for clarity. The sample sits on a copper block clamped to a PID-controlled Peltier cooler. This assembly is mirrored across the sample to form the complete assembly. (b) The complete assembly delivers a temperature gradient via two Peltier coolers on either side of the sample. The hot side of each Peltier cooler is mounted to a large water-cooled aluminum heat sink. The top half of the assembly clamps down on the bottom half via threaded guide rods to ensure excellent thermo-mechanical contact between the sample and copper blocks.

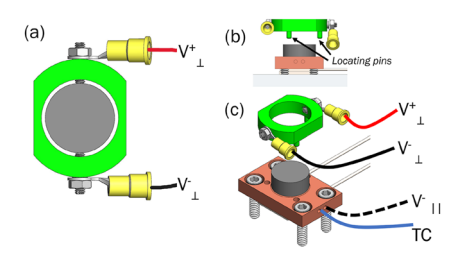


FIG. 3. (a) The 3D-printed voltage ring (green) is custom designed to ensure coplanar electrical contacts for a transverse (denoted by V_\perp) Nernst measurement. Brass set screws fasten via heat-set threaded inserts to form point contacts with the sample, as shown in the figure. (b) The locating pins of the voltage ring interface with mating holes on the bottom copper block to ensure correct installation and direction of polarity. (c) The type T thermocouple (TC) is clamped into the copper block via a set screw on the underside of the copper block (not visible in the figure) to ensure excellent thermal contact between the TC bead and the copper block. The dashed line (V_\parallel^-) shown in (c) indicates the wire used for measuring magneto-Seebeck; a mirrored wire is located in the top copper block (not shown in the figure).

heater/cooler blocks (Fig. 2), which are machined from copper to efficiently conduct heat to or away from the sample. Each copper block (5 × 20 × 32 mm) has a square recess (0.5 mm deep, not visible in Fig. 2) machined to receive the cold side of a Peltier module (CUI Devices CP60133, $Q_{\rm max}$ 12.2 W at 27 °C). For a sample of ~12 mm diameter and ~5 mm tall [an elongated version of the disk shaped samples commonly produced from hot pressing and spark plasma sintering, Fig. 1(a), l_x = 5.0 mm and l_y = 12 mm] with a thermal conductivity of 3.0 W m⁻¹ K⁻¹, the heat requirement at room temperature to deliver a ΔT of 5 K across the sample is only 0.34 W from Fourier's law. It takes us less than 1 min to establish a ΔT of 5 K at room temperature for a variety of materials with thermal conductivities ranging from 2 to 10 W m⁻¹ K⁻¹. The hot side of the Peltier is heat sunk to an aluminum water-cooled block (Fig. 2). Thermal grease is applied to either side of the Peltier module

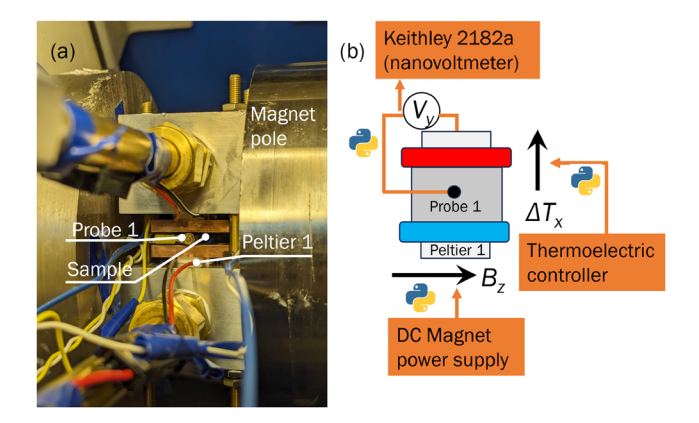


FIG. 4. (a) The sample is sandwiched between two Peltier/copper/aluminum block assemblies that differ only in the width of the aluminum block. The top block is 5 mm narrower, permitting easy removal, while the lower block stays clamped in place between the magnet poles. Probe 1 refers to one of the voltage probes that touches the sample and measures the Nernst voltage. The other probe is located on the back side of the sample and is not visible in the photo. The black and red leads visible in the photo provide DC power to the Peltier modules (Peltier 1). (b) Instrumentation schematic showing each hardware component involved in generating and measuring $N = \frac{E_y}{\nabla_x T B_z}$. The orientation and labels (Probe 1, Peltier 1) of the cartoon match the photo (a). The nanovoltmeter, thermoelectric controller (TEC), and DC magnet source all interface with a computer (not shown) and communicate via Python. The actual calculation of the Nernst coefficient is automatically performed by our Python script, minimizing human error.

to improve contact between the interfaces. The bottom aluminum heat sink block is 55 mm wide (along the *z*-direction, Fig. 2) and is directly clamped between the pole caps of the magnet [Fig. 4(a)]. The upper heat sink block is 50 mm wide, which allows the lower block to remain clamped while the upper block can be easily removed to load samples.

2. Excellent thermal contact

Minimizing the thermal contact resistance between the sample and heater/cooler blocks is paramount for estimating the thermal gradient within the sample. The primary source of this thermal contact resistance is expected to be due to the microscopic gaps between the surface of the pellet and the copper stage of the Nernst instrument. This is addressed by a combination of compression and filling interfacial gaps by placing a thin piece of graphoil between the two surfaces before applying compression. Threaded guide rods pass through the aluminum blocks [Fig. 2(b)] and serve two functions: (1) to precisely locate the top block on top of the sample, and (2) to ensure excellent thermal contact with the sample; when the nuts are tightened on the installed rods, the blocks firmly press against the sample [Fig. 2(b)]. This design thus encourages uniform thermal contact resistance. Coupled with the copper blocks serving as effective heat spreaders, the expectation is that the boundary conditions on the sample are uniform laterally and that a 1D heat flow approximation can be made. This one-dimensional heat flow approximation is successfully employed in uniaxial Seebeck measurement systems.²⁸

3. Accurate control and measurement

Measurement and control of the thermal gradient are performed via a multi-channel thermoelectric controller (TEC) from Meerstetter Engineering with bipolar DC output to the Peltier coolers. The TEC contains PID controllers, which dictate the current output to the independent Peltier modules. The copper heater/cooler blocks sandwich the Peltier cooler to the aluminum heat sink block; nylon screws are used to clamp the blocks to avoid thermally shorting the copper block to the aluminum heat sink block. Within the copper block is a machined hole that sits 1.25 mm beneath the sample and receives the thermocouple bead. Our (type T) thermocouples are made of spot welded, sheathed copper and constantan wires. Thermocouples should be made from extremely fine wires (e.g., California Fine Wire) as a matter of best practice. We employ an exposed junction thermocouple for fast response time. The temperature we measure at the copper block is the temperature used to drive the desired ΔT across the sample, as described in Sec. III. Measuring the temperature at the copper blocks is an accurate proxy for sample temperature due to the small Seebeck coefficient and colossal thermal conductivity of copper. To demonstrate this, we measure the Seebeck effect using copper wires also embedded in the copper blocks [Fig. 3(b), V_{\parallel}^{-}], and we achieve accurate values (Fig. 7). By measuring the sample temperature indirectly, we free up space on the sample for transverse voltage probes as well as avoid unwanted heat transfer between the sample and the thermocouple (i.e., the "hot" or "cold finger" effect).

B. Voltage measurement

Our electrical design achieves accurate voltage measurements without compromising usability. For accurate measurements, the probes must be highly electrically conductive, possess a low Seebeck coefficient, be non-magnetic, form point contacts on the sample, and be located perpendicular to the temperature gradient and magnetic field. Furthermore, we seek usability. Our design goals for enhancing instrument usability include ease of contacting the sample with probes, automatic alignment along the *x*-axis to avoid spurious thermally induced voltages (discussed in detail in Sec. III C), and probes that are mechanically stable and chemically inert. In brief, we use a 3D printed voltage probe ring with embedded brass set screws to form point contacts on the sample (Fig. 3) at a prescribed height and alignment.

1. Geometry constraints for electrical contacts

The geometry constraints that must be satisfied to measure the Nernst voltage warrant further detail. In general, voltage probes should form point contacts with the sample when performing an electrical measurement. Point contact geometry is satisfied by using small (M2) brass flat-tipped set screws that press into the side of the sample (Fig. 3). The diameter of the set screw tip is much smaller than the height of the sample. Specific to Nernst, the electrical contacts must be co-planar with the yz plane (i.e., perpendicular to the temperature gradient along the x-direction). To ensure that the set screws are co-planar, we designed and 3D printed a retainer ring that pins the two electrical contacts to the same height (in the x-direction). The 3D printed ring is electrically insulative to avoid shorting the two contacts and can be readily manufactured. The set screws thread into heat-set threaded inserts, chosen to be of the same

material as the screws to avoid thermal EMFs at the thread/screw interface. The inserts are easily installed (only once) with a soldering iron and allow for easy insertion/removal of the set screws. While not implemented here, higher temperatures could be probed through the use of rings based on fluoropolymers, machineable glass ceramics, or boron nitride.

2. Complete electrical circuit: Sample to nanovoltmeter

Next, we describe the electrical connections between the sample and the nanovoltmeter [Fig. 4(b)] and the process of making electrical contact with the sample prior to performing each measurement. Starting from the sample, one end of the brass set screw is pressed into the sample to ensure excellent electrical contact. The other end of the set screw is equipped with a brass M2 nut that clamps a copper ring terminal crimped to a copper wire (Fig. 3). Each copper wire is joined to a LEMO cable [obeying the Gerlach convention for voltage polarity, Fig. 1(a)] emanating from the nanovoltmeter via a set of terminal blocks. While we have done our best to minimize the number of electrical junctions, especially those consisting of dissimilar metals—these unavoidable junctions can lead to unwanted thermal offset EMFs, which will be discussed in Sec. III.

3. User experience

The process of making electrical contact with the sample for a measurement is quite easy. The sample is placed in the recessed portion of the copper stage [Fig. 3(c)] and the 3D printed voltage retainer ring is placed around the sample. The keyed design of the voltage ring ensures that it can only be installed one way. Three locating pins (two in the front and one in the back) interface with corresponding holes on the copper block [Fig. 3(b)]. The pins ensure that the voltage probes are located at the same point every time, that the measured voltage is perpendicular to the plane of the electric field, and that the correct polarity is measured. Once the voltage ring is firmly seated, the set screws are fastened until they make good contact with the sample, and the nuts are tightened. The top heater/cooler block is installed along the guide rods and clamped down. After the Nernst measurement is complete (Sec. III), the nuts are loosened and the screws are backed out. The ring and its accoutrements (Fig. 3) are indefinitely reusable until a component breaks, and the replacement of any component is inexpensive in both time and labor. The sample contact making process thus takes less than a minute, which is extraordinary in the world of electrical and especially thermomagnetic measurements. In addition, the thermocouples are permanently embedded in the copper blocks directly under the sample [Fig. 3(c)].

C. Magnet

1. Magnet considerations

Some of the considerations for the magnet used for a Nernst measurement include the desired field strength, the ability to vary the field strength, and the pole gap, which dictates the distance to fit the sample holder assembly. While the particular method to deliver ΔT varies across Nernst instruments, all designs are united by the constraint that the sample holder must fit within the poles of a magnet or the bore of a superconducting coil. Regarding the required

field strength, for a low field Nernst measurement [μ B \ll 1, recall μ : mobility (m²/V s), B: magnetic field (T)], a magnet that can achieve 1 T is quite sufficient for most thermoelectric materials. An electromagnet has the advantage of a relatively larger pole gap and ease of reversing field direction as compared to a permanent magnet.²6 The ability to control the field in steps allows for more accurate measurements than transient measurements at the expense of equilibration time.

2. Calibration

To calibrate our magnet, we installed a gaussmeter where the sample sits. We kept all of the wires and sample holder components in place during our calibration to get an accurate environment for what our sample experiences. While we specifically chose materials with low magnetic susceptibility, we wanted to ensure that our gaussmeter experienced the same electromagnetic environment as our sample during measurement. We then applied a DC current to the magnet at linear increments up to 50 amps and reversed the polarity, recording the field at each step. The resulting dataset is linear (r = 0.9998) and shown in Fig. S3. Our maximum field is achieved at 55 amps, which corresponds to 0.935 T. In practice, we typically sweep up to 50 amps.

D. Comparison to other Nernst instruments

Having introduced our embodiment, we compare and contrast the design to other reports in the field. In this discussion, we will focus on (i) electrical contacts, (ii) sample geometry, (iii) heat flow geometry and thermal management, and (iv) thermometry.

1. Electrical contacts

Concerning electrical contacts, the literature to date has focused on wire-bonding or other adhesion-based approaches to attach contacts to the sample. ^{6,8,22,25,29,30} One notable exception is the on-chip lithographic lead fabrication employed by Wu *et al.* ²⁹ Our approach focuses on mechanical removable contacts constrained within a ring to improve alignment, ease of application, and resiliency [Fig. 3(a)].

2. Sample geometry

The sample geometry in the literature varies widely, with thin films, 6,21,29 parallelepiped bars, 8,22,24,25 and single crystal measurements 30 reported by various groups. Thin-film samples have the advantage of lithographic techniques to pattern geometries to maximize the Nernst voltage, avoid unwanted spurious voltages, 6 and even fabricate on-chip electrical leads for the sample. 29 Within the context of bulk materials, we have found that the cylindrical geometry is appealing due to the limited modifications required for a uniaxially pressed sample. Through the use of our voltage probe ring [Fig. 3(a)], we are able to easily measure the voltage V_y and calculate l_y as simply the diameter of the sample.

3. Heat flow geometry and thermal management

Establishing a well-defined thermal gradient in a bulk material is challenging, and multiple sample holder geometries are found in the literature. For example, a sandwich geometry is sometimes used, with heaters on the y–z faces [i.e., faces normal to the heat flow direction, Fig. 1(a)]. ^{8,30} This is attractive as it facilitates pseudo-one dimensional heat flow. However, other approaches apply heat in a

"bridge" geometry, with heat being applied and removed at the ends of the x-y face. 6,22,25 This approach is effective for thin film samples but may lead to errors in the temperature gradient in thicker samples due to thermal gradients in the z-direction. Here, we have utilized the sandwich geometry with active cooling and heating; this has several benefits: (1) active cooling at one end of the sample allows us to focus on using a geometry that optimizes signal and accuracy rather than worrying about dissipating sufficient heat flux, (2) supplying the temperature gradient across the faces of the sample (sandwich geometry) clearly defines the l_x portion of $\nabla_x T$ (accurately determining l_x can be a challenge 25), and (3) the use of active cooling on the cold side lends itself to an extremely controllable and stable ΔT . This last point is in contrast to the vast majority of systems that simply use heat baths to passively remove heat, rendering control of ΔT difficult.

4. Thermometry

In the Nernst literature, there seems to be a broad consensus that accurate thermometry is challenging.^{8,25,29} Correctly determining the temperature gradient at the sample requires decisions concerning thermocouple placement and environment. Specific concerns include thermal contact resistance, associated hot/cold finger effects, and estimation of l_x . Wu et al. resolved these conflicts in their Nernst measurement device by fabricating on-chip thermometers from indium oxide.²⁹ This is an innovative approach to optimize thermal contact between the thermometer and the sample; however, it requires lithography (not applicable to bulk materials), and systematic errors are introduced when translating the current to a temperature using a linear approximation.²⁹ Universally, thermal contact resistance between the sample and thermometer leads to errors in the ΔT used to estimate $\nabla_x T_i^{30}$ our system embeds the thermocouples in copper blocks to increase the contact area.³¹ Another concern is hot/cold finger effects; this is mitigated in the Wu design as well as in designs where the thermocouple is attached to a copper plate thermally sunk to the sample⁸ or the thermocouple is threaded through the primary stage heater.²⁵

III. MEASUREMENT

Having discussed our hardware embodiment, we move on to our measurement protocol. The Nernst measurement consists of multiple voltage readings in a constant temperature gradient as the magnetic field is swept from a negative to a positive field. In this section, we describe our measurement procedure to calculate the Nernst coefficient with minimum uncertainty and error. Along the way, we correct for assumptions and unwanted voltages from competing transport phenomena. We also discuss what types of materials are good candidates for Nernst measurements and their ideal geometry to generate the largest possible signal.

A. Materials studied

We provide demonstration measurements for three different materials with diverse electronic properties. Degenerate p-type SnTe, intrinsic n-type InSb, and semimetal Bi are all synthesized using typical solid state techniques and uniaxial hot pressing to form dense polycrystalline pellets for electronic measurements. The dimensions of the samples are $l_x = 6.327$ mm, $l_y = 12.9$ mm (SnTe); $l_x = 8.150$ mm, $l_y = 12.9$ mm (InSb); and $l_x = 7.160$ mm, $l_y = 13.0$ mm

(Bi). Knowledge of these dimensions is required to calculate the Nernst coefficient [Eq. (2)]. The dimension l_y is set by the diameter of the hot press die, and therefore, this dimension is similar between samples.

These materials were selected for their relevance to the thermoelectric community as well as their excellent room temperature mobility. At 50 °C, Hall mobility values measured on our high temperature Hall effect apparatus²⁶ are the following: 466 cm²/V s (SnTe), -786 cm²/V s (InSb), and -3170 cm²/V s (Bi). While these are high electronic mobility values, they still fall under the low magnetic field regime up to 1 T. Hall carrier concentrations at 50 °C are 1.09×10^{20} cm⁻³ (SnTe), -1.58×10^{17} cm⁻³ (InSb), and -1.27×10^{19} cm⁻³ (Bi). We calculated these carrier concentrations from $R_H = \frac{1}{ne}$, where e is the fundamental charge, n is the Hall carrier concentration, and R_H is the measured Hall coefficient. Mobility μ values were derived using the Drude theory $\frac{1}{\rho} = ne\mu$, where ρ is the measured electrical resistivity. Resistivity values measured at 50 °C are 50.45 mΩ-cm (InSb), 0.13 mΩ-cm (SnTe), and 0.16 mΩ-cm (Bi). Seebeck coefficient values are shown in Fig. 7.

B. Measurement sequence

The low field Nernst coefficient (N) measurement is carried out in a thermal gradient applied along the x-axis of the sample in a variable magnetic field (z-axis).

1. Set temperature gradient

First, a ΔT of 1–5 K (higher magnitude for low mobility samples to drive a detectable voltage) is applied via the thermoelectric controller [Fig. 5(a)]. A desired average temperature and ΔT are input to our software program (all done in Python), and the upper and lower temperatures are automatically calculated and sent to the controllers [i.e., an input of $\bar{T} = 20$ °C, $\Delta T = 5$ K, will drive the top block to 22.5 °C and the bottom block to 17.5 °C, Fig. 5(a)]. The two Peltier coolers are driven to the required set points and equilibrated for 45 s. Our 1D heat flow modeling in COMSOL suggests that for a 6 mm long sample with a thermal conductivity of 3 W m⁻¹ K⁻¹ (i.e., SnTe), the temperature gradient will be established within 10 s (Fig. S1). Since this is calculated with many approximations (*dT* is set as a boundary condition at sample edges rather than at the copper blocks in actuality), we allow ample extra time for equilibration. Our measurements show temperature fluctuations on the order of mK (Fig. S5). Nernst measurements are fundamentally different from Seebeck measurements in that the Seebeck measurement is resilient against non-linear temperature profiles when the sample is homogeneous; this is not the case for Nernst measurements.

2. Step the magnet field

Once the ΔT has equilibrated for 45 s, current is sent to the magnet to drive a field of -1 T [Fig. 5(b)]. Once the field has settled, the induced transverse sample voltage is measured by the nanovoltmeter [Fig. 5(c)]. Then, the magnetic field is incremented in user-specified linear steps up to +1 T, and the nanovoltmeter measures voltage along the way [Figs. 5(b) and 5(c)]. We note that we wait for the magnetic field to stabilize at each step, sacrificing acquisition time in order to maximize accuracy. To verify that our field sweep rate is not too rapid, we performed additional measurements at a significantly reduced rate and achieved the same value N (Fig. S6).

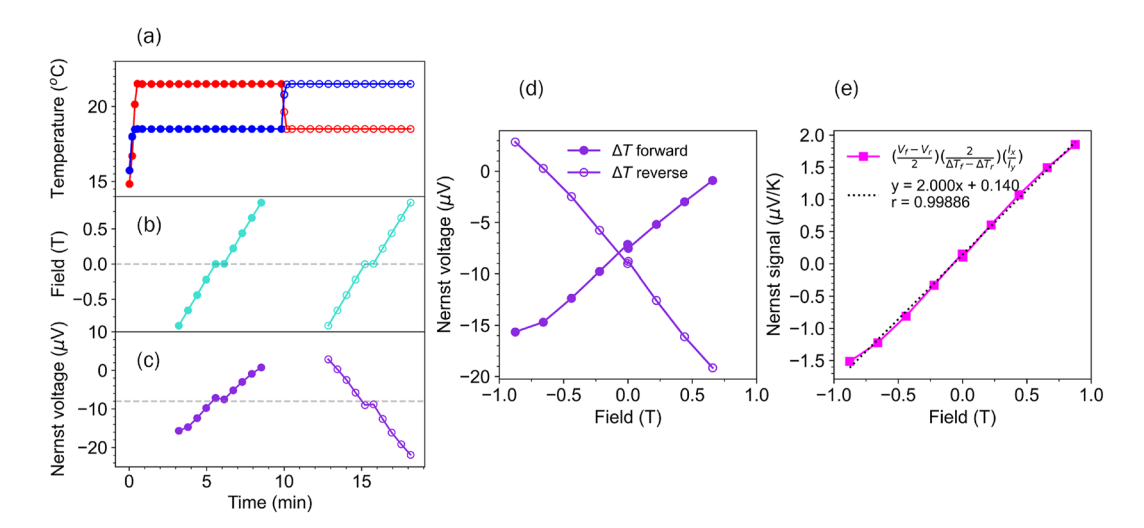


FIG. 5. (a)–(c) We show the process of measuring the Nernst coefficient on a sample of polycrystalline SnTe at $\overline{T}=20\,^{\circ}\text{C}$ as a function of time. (a) First, we establish a static $\Delta T=3\,^{\circ}\text{C}$. (b) Once the thermal gradient has equilibrated across the sample, we apply a magnetic field in steps to yield (c) Nernst voltage measurements at each magnetic field value. The temperature gradient is reversed once the full range of magnetic fields has been swept (\approx 10 min). (d) The raw Nernst voltages (μ V) for the forward and reverse temperature gradients are plotted as a function of magnetic field (T). These data are simply the points from (c) plotted as a function of the field. (e) The Nernst coefficient is the slope of the Nernst signal data (μ V/K): $N=2.0\,\mu$ V/KT for this SnTe sample.

3. Measure voltage

Under low magnetic fields, the Nernst voltage is a linear function of the field.⁵ From the field-dependent voltage measurements taken at a constant ΔT (Fig. 5), we are able to calculate the low field Nernst coefficient,

$$N = \frac{\Delta V_y}{\Delta B_z} \frac{l_x}{\Delta T_x l_y}.$$
 (3)

By measuring the voltage at different field values, we are able to calculate $\Delta V/\Delta B$. This slope method has the benefit of effectively canceling out any Seebeck voltages or other offset voltages that contribute to our Nernst measurement, assuming the Seebeck offset is an even function of the field (Fig. 6). Any thermal EMFs that may arise due to temperature differences along the wires will be canceled out via our differential measurement.

4. Reverse temperature gradient

Our instrument's design allows us to easily reverse the direction of the temperature gradient. By reversing the direction of ΔT and taking an average (paying attention to polarity) of the $\Delta V/\Delta B$ for the forward and reverse temperature gradient measurements, we effectively cancel out thermal EMF offsets. This is akin to the DC reversal or delta method commonly performed in Hall and resistivity measurements. ^{26,32,33} The voltage data recorded for the forward and reverse ΔT are shown in Fig. 5(d) and, as expected, have opposite slopes. Of note, at zero field, some offset is present in the data. This offset will be discussed in detail in Subsection III B 5.

5. Treatment of offset voltages

At B = 0, the measured Nernst voltage should be 0 V in theory [Eq. (1)]. However, this is not the case in practice, ⁸ as evidenced

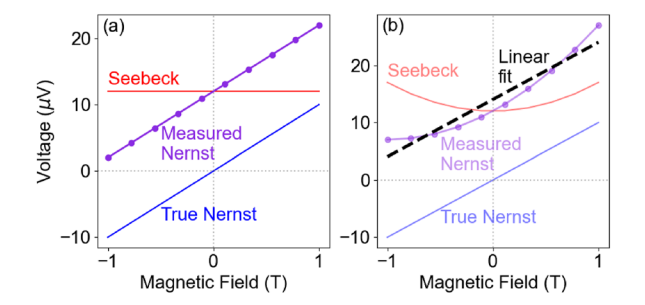


FIG. 6. Deriving the Nernst coefficient N from dV/dB is a technique that leads to accurate N even when offsets from Seebeck are present. (a) If the Seebeck effect has a weak or zero magnetic field dependence (red trace), the measured Nernst voltage (purple) will pick up a linear offset from the theoretical value (blue) if the probes are slightly offset. The accurate N will still be determined. (b) In the case of field dependence for the Seebeck coefficient, the measured Nernst voltage (purple trace) is no longer linearly offset but is a combination of the odd Nernst function and even the magneto-Seebeck function. However, a linear regression through the measured data (symmetrically sampling both positive and negative field values) will yield the correct dV/dB and, therefore, N.

herein [Figs. 5(c) and 5(d)]. In this subsection, we will explain why these offsets are not overly problematic.

The measurement of the Nernst voltage includes not only the desired voltage but also the Seebeck voltage due to any misalignment in the voltage probes and any other thermal EMFs or noise in the circuit. Considering Fig. 5(c) at B=0 (minutes 5.5 and 15.5), the voltages are -7.3 and $-8.9~\mu V$ for the forward and reverse temperature gradients. Treating the voltage offset as a combination of two linear terms, one of which depends on the sign of the temperature gradient, we conclude that the majority of the offset ($-8.1~\mu V$)

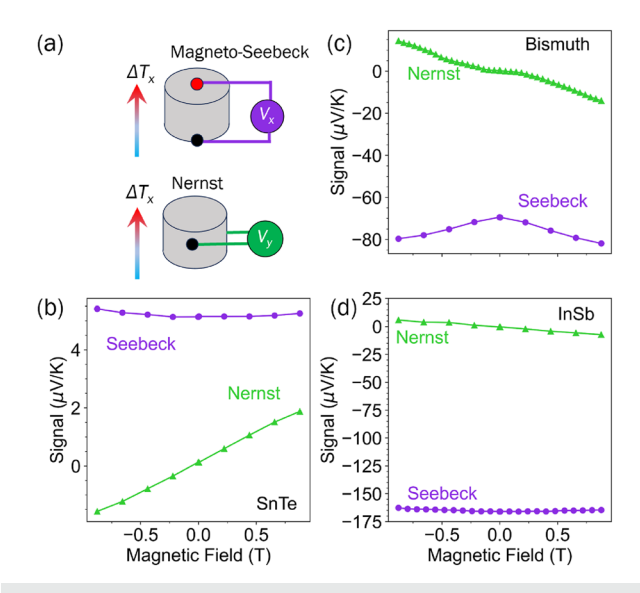


FIG. 7. (a) Schematics demonstrating longitudinal vs transverse probe placement to generate the data in (b)–(d): for a Seebeck measurement, the probes are located along the same direction as the temperature gradient (V_x), and for a Nernst measurement, the probes are located transverse to the temperature gradient (V_y). (b)–(d) Magneto-Seebeck and Nernst signal data shown at 20 °C ($\Delta T = 5$ K) for bulk polycrystalline samples of SnTe, Bi, and InSb. At zero field, the Nernst signal in all materials is zero, as expected. The Nernst *coefficient* (μ V/KT) is, therefore, calculated from the slope of these plots: (b) SnTe ($N = 2.0 \ \mu$ V/KT), (c) elemental bismuth ($N = -6.4 \ \mu$ V/KT; fitted through the linear region between -0.2– $0.2 \ T$), we show data with tight spacing to higher field in order to highlight the loss of linearity (high field conditions) above \sim 0.2 T (fitting through +/-1 T would incorrectly result in a coefficient of $-15 \ \mu$ V/KT), and (d) InSb ($N = -7.6 \ \mu$ V/KT).

is independent of the temperature gradient. The Seebeck voltage is only 0.8 μ V; this provides direct insight into the probe offsets. The corresponding probe offset along the *x*-direction is $l_{\rm offset} = \frac{V_{\rm offset}}{E_S} = \frac{0.8~\mu V}{2.4 \times 10^{-3}~\rm V/m} = 0.33$ mm, where E_S refers to the Seebeck electric field. For $S_{\rm SnTe} = 5~\mu V/\rm K$ [Fig. 7(c)], $E_S = \frac{V_s}{l_x} = \frac{S\Delta T}{l_x} = \frac{5~\mu V/\rm K \times 3~K}{6.3~\rm mm} = 2.4 \times 10^{-3}~\rm V/m$. This $l_{\rm offset}$ is significantly smaller than the height of the pellet ($l_x \approx 6~\rm mm$), highlighting the excellent alignment of the two probes.

To further investigate the role of probe misalignment, we took additional measurements at various ΔT and saw that the relationship between dV/dB and ΔT is linear and nearly pierces the origin (Fig. S7). This indicates that our measurement procedure is effective at canceling out thermal offset voltages. In conclusion, our measurement procedure of extracting the Nernst coefficient from the slope of dV/dB effectively cancels out both thermal EMF offsets and Seebeck offset voltages.

C. Magneto-Seebeck coefficient measurement

Measuring the magneto-Seebeck coefficient can be useful for understanding charge carrier transport in a given material in addition to the Nernst coefficient. Our measurement protocol consists of (i) moving the voltage probes from a transverse (Nernst) to a

longitudinal configuration along the sample [Fig. 7(a)] and (ii) performing dV/dT measurements at different B fields. Each copper block [Fig. 2(a)] has a small drilled hole directly under the sample. To measure the magneto-Seebeck voltage, we insert copper wires into these holes [Fig. 3(b)] and connect them to the Keithley 2182 nanovoltmeter. In this way, we measure the voltage longitudinally, taking advantage of the high electrical conductivity and low Seebeck coefficient of copper.

While both the Nernst and the magneto-Seebeck measurements use a differential method to eliminate offsets and calculate the desired coefficient, the protocol differs in what is swept and what is held constant. For the Nernst measurement, we apply a constant ΔT and sweep the field (Fig. 5), and for the magneto-Seebeck measurement, we hold the field constant and sweep ΔT . In Fig. 7, each data point represents a slope $\Delta V/\Delta T$ at a given field. The procedure of sweeping ΔT and recording $\Delta V/\Delta T$ to obtain the Seebeck coefficient is quite common and considered to be more accurate than other methods. ^{22,27,28} As was the case for measured Nernst voltage vs field [Fig. 5(d)], non-linearity in $\Delta V/\Delta T$ for Seebeck may suggest poor contacts, a poor signal, or both. ^{22,27,28}

In the absence of a magnetic field, misalignment of the Nernst probes will induce a small Seebeck voltage due to the ensuing ΔT_x ; as discussed above, this can be eliminated through a differential $[\Delta V/\Delta B,$ Eq. (3)] Nernst measurement. In the case where the Seebeck response is an even function of the magnetic field, a linear regression of the resulting curve will continue to preserve the true Nernst value, provided that both positive and negative magnetic field values are sampled evenly [Fig. 6(b)]. However, if the magneto-Seebeck response is not an even function, this approach will not work, and its contribution cannot be simply removed from the Nernst voltage by calculating $\Delta V/\Delta B$. As real samples may show anisotropic transport, the magneto-Seebeck response may not be a perfectly even function, and we generally recommend determining the magneto-Seebeck response when analyzing experimental Nernst data.

D. Sample property considerations

The need to measure nV to μ V signals distinguishes the Nernst effect from more common electronic transport measurements, which typically involve measuring voltages that are orders of magnitude higher, such as electrical resistivity, Seebeck, and Hall.⁶ The difficulty in measuring petite Nernst signals is exacerbated in samples with low electronic mobility. In this section, we provide an overview of the fundamental physics that contributes to a detectable Nernst signal and, therefore, what material properties must be in place for a detectable Nernst measurement.

Several formalisms describe the Nernst effect and aid the reader in understanding what material properties are required for a detectable Nernst signal. $^{1,3-5,8,16}$ The solution of the Boltzmann equation (independent of single parabolic band assumptions) yields the following relationship between Nernst and mobility: $N \propto \frac{\tau_0}{m^*}$. Therefore, high electronic mobility is necessary to generate a detectable Nernst signal since μ is proportional to $\frac{\tau_0}{m^*}$. In practice, measuring the Nernst coefficient on samples with mobility values <50 cm² V⁻¹ s⁻¹ can be challenging. We add that this heuristic approach depends on the energy dependence of scattering. In short, thermoelectric materials suffering

from low mobility due to extensive defect engineering to decrease their thermal conductivity might not be good candidates for Nernst measurements.

Low thermal conductivity, on the other hand, is a desirable feature. This lowers the heat requirement to impose a dT across the sample. It also increases the amount of time required for equilibration. Beyond low total thermal conductivity, specifically the ratio of lattice thermal conductivity (κ_L) to electronic thermal conductivity (κ_{el}), it is important to encourage isothermal conditions. High κ_L relative to κ_{el} helps avoid adiabatic conditions, wherein the phonons act as a "shorting fluid" if a temperature gradient tries to develop along the y-direction to cause a thermal Hall effect.⁵

Finally, we consider the case of bipolar materials. While bipolar materials are not desirable for Seebeck-based thermoelectric applications, they actually lead to a larger Nernst signal than materials with one dominant carrier type. For example, the large Nernst signal in kagome superconductor CsV_3Sb_5 is attributed to its ambipolar nature and the presence of hole-like *and* electron-like bands at critical points in the Brillouin zone.^{17,34} This is due to the heightened voltage generated by electrons and holes traveling in the same direction (from the thermal gradient) but curling in opposite directions (in a magnetic field).^{16,17} This differs from the Hall effect, where charge carriers travel in opposite directions (from the electrically generated field) and curl in opposite directions, effectively ending up on the same side of the material and canceling each other out.

In summary, high electronic mobility is a prerequisite for a good Nernst measurement. In addition, low thermal conductivity and ambipolarity are beneficial material properties for Nernst measurements. Examples of materials with high Nernst coefficients are bismuth, InSb, and NbSe₂, all of which possess excellent electronic mobility. ^{8,16,22}

E. Sample geometry

The ideal sample geometry for a Nernst measurement should be considered from two perspectives: (1) maintaining isothermal conditions, and (2) maximizing the measurable Nernst voltage. Under assumed isothermal conditions, the only temperature gradient present in the sample during a Nernst measurement is along the x-axis. However, a temperature gradient in a magnetic field can give rise to an additional temperature gradient ($\nabla_y T$) generated by the thermal Hall effect. If $\nabla_y T$ develops, then adiabatic, not isothermal ($\nabla_y T = 0$) Nernst is measured. That is, an additional voltage develops along the y-axis due to the Seebeck effect ($V_y = \Delta T_y S_{yy}$). In reality, some medium between pure isothermal or adiabatic conditions is likely to be met in most Nernst measurement systems.

We acknowledge that our relatively short, squat pellet geometry differs from the long, skinny samples often utilized for Nernst measurements. Separate This difference is enabled by our active cooling (Peltier cooler), which allows for a squat geometry along l_x while maintaining a large ΔT . In addition, embedding thermocouple wires in the copper blocks avoids needing space for multiple contacts to the sample along l_x [Fig. 3(c)]. For our pellet geometry [Fig. 3(b)], adiabatic conditions are avoided by minimizing the pellet height to ensure maximum pellet surface area is in contact with the copper

heat spreaders. While a short sample is valuable in terms of maintaining isothermal conditions in y, this places further demands on the overall thermal circuit in x. In particular, maintaining a large ∇T becomes challenging as more heat is required to maintain a temperature difference across a thin sample. Furthermore, the thermal contact resistance between the copper blocks and the sample may begin to represent a nontrivial fraction of the overall thermal resistance. For researchers studying the Nernst effect in long (along the axis of temperature gradient), thin samples, isothermal assumptions may not be accurate. One conversion from the low field adiabatic to the isothermal Nernst coefficient may be difficult and require measurement of other galvano-thermomagnetic phenomena to apply the Heurlinger relations.

Now that we have considered how maximizing sample surface area in contact with the heating/cooling blocks encourages an isothermal regime, we turn to sample geometries that generate the highest Nernst voltage. As shown in Eq. (2), the Nernst voltage V_y scales with $\frac{l_y}{l_x}$. The l_y dimension [Fig. 1(a)] is limited by the diameter of the die from which it was pressed. Therefore, maximizing this dimension is difficult without changing the internal dimensions of the hot press die. However, l_x is the pellet thickness [Fig. 1(a)], and this can be easily manipulated by sanding/polishing the faces of the pellet to reduce its thickness. Minimizing l_x for a given l_y should increase the measured Nernst voltage [Eq. (2)]. Our results in Fig. S4 of the supplementary material show that increasing the ratio l_y/l_x did, in fact, increase the measured Nernst voltage. The Nernst coefficient (Fig. S4) is unchanged as expected since N is an intrinsic property.

We have considered the sample geometry now from two different perspectives: (1) maintaining isothermal measurement conditions and (2) maximizing the Nernst voltage (Fig. S4). As a reminder, a sample that is thin along the direction of the temperature gradient (l_x) encourages isothermal conditions by maintaining a greater sample surface area in contact with the copper heat blocks. The ideal geometry to maximize the Nernst voltage also benefits from a thin l_x since $V_y \propto \frac{l_x}{l_x}$ [Eq. (3)]. Therefore, we use the minimal thickness l_x [Fig. 1(a)] pellet to maximize the Nernst voltage. For our system, this corresponds with a sample at least 5.1 mm thick because our plastic voltage ring assembly [Fig. 3(b)] is 5 mm thick.

F. Measurement uncertainty

The origins of uncertainty in our Nernst coefficient measurements could arise from the measurement hardware (nanovoltmeter, thermocouples, magnet, thermal equilibration between sample holder and sample) or from imprecise sample geometry measurement [Eq. (3)]. Our efforts to quantify this unavoidable uncertainty consist of performing a root-square-sum (RSS) [Eq. (4)] on the primary sources of uncertainty.

Inspection of Eq. (3) reveals the primary sources of uncertainty in a Nernst measurement. The sources we used, which correspond to the standard deviation σ_i in Eq. (4), are (i) repeated measurements of the Nernst coefficient itself, (ii) uncertainty in l_x , and (iii) uncertainty in l_y . The Nernst coefficient (μ V/KT) measurement embodies error from thermometry, the voltmeter, and the magnet. To quantify the uncertainty in the Nernst measurement, we repeated 26 Nernst coefficient measurements on the same sample of SnTe at $\overline{T} = 20\,^{\circ}$ C

over the course of a week. The average value was 2.014 μ V/KT, and the sample standard deviation was 0.023 μ V/KT. For the sample geometry (ii) and (iii), we determined the actual tolerance range, which was 0.050 mm for l_x (sample height) and 0.10 mm for l_y (sample diameter).

The total standard deviation (uncertainty) is

$$\sigma_{total} = N\sqrt{\sum \sigma_i^2}.$$
 (4)

Using Eq. (4), we calculate a σ_{total} of 0.052 μ V/KT for N=2.014 μ V/KT. This agrees well with the experiment—the standard deviation taken from repeated measurements on the same sample (over the span of several days) is $\sigma=0.023~\mu$ /KT.

A final note—the lack of a calibration standard for Nernst coefficient measurements makes absolute error analysis difficult in reference to a calibrated standard. However, we are most interested with trends within a given experimental campaign. As such, we are most concerned with the precision rather than error minimization of our measurement collection sequence.

IV. FUNDAMENTAL THEORY AND ANALYSIS

In the Introduction, we discussed the physical origin and the significance of the Nernst effect measurement. We stated that within the single parabolic band regime, Nernst measurements can be analyzed using the method of four coefficients to determine the dominant carrier scattering mechanism in a conductive material. In this section, we describe in more detail how this is done, starting with the macroscopic picture and then diving into the underlying transport physics that can be used to analyze Nernst data.

On a macroscopic level, the coupled current equations explain the relation between measurable electronic and heat currents (J_e and J_q) and the force and field vectors that generate these currents. Here, we will focus on the electronic current J_e ,

$$I_e = \overline{\sigma} \cdot E - \overline{\alpha} \cdot \nabla T. \tag{5}$$

Writing out the full tensor and asserting that there is a magnetic field applied along the z-direction, 36 we obtain

$$\begin{pmatrix}
J_{x} \\
J_{y} \\
J_{z}
\end{pmatrix} = \begin{pmatrix}
\sigma_{xx} & \sigma_{xy} & 0 & \alpha_{xx} & \alpha_{xy} & 0 \\
\sigma_{yx} & \sigma_{yy} & 0 & \alpha_{yx} & \alpha_{yy} & 0 \\
0 & 0 & \sigma_{zz} & 0 & 0 & \alpha_{zz}
\end{pmatrix} \begin{pmatrix}
E_{x} \\
E_{y} \\
E_{z} \\
-\nabla_{x}T \\
-\nabla_{y}T \\
-\nabla_{z}T
\end{pmatrix}.$$
(6)

The electric and thermoelectric conductivity tensors $\overline{\sigma}$ and $\overline{\alpha}$ have on-diagonal components that can be probed via longitudinal measurements (i.e., resistivity, Seebeck), and the off-diagonal components $(\sigma_{ij}, \alpha_{ij}, i \neq j)$ are zero in the absence of a magnetic field (for an isotropic material; notwithstanding interesting cases such as materials exhibiting axis-dependent conduction polarity³⁰).

Before applying Eq. (5) to Nernst measurements, we consider the simpler case of a Seebeck measurement. Here, a temperature gradient is applied only along the x-axis of a material, and there is no applied magnetic field. Under an open circuit boundary condition ($J_x = 0$), the first row of Eq. (5) becomes

$$J_x = \sigma_{xx} E_x - \alpha_{xx} \nabla_x T = 0. \tag{7}$$

The material property that describes the drift of electrons due to a temperature gradient (thermoelectric conductivity¹⁰) is α_{xx} . The more familiar electrical conductivity associated with an applied electric field is denoted by σ_{xx} . Thus, an electric field is generated to balance the diffusion of charge carriers due to the temperature gradient. Equation (7) can be rearranged to yield the longitudinal Seebeck coefficient S_{xx} ,

$$\frac{\alpha_{xx}}{\sigma_{xx}} = \frac{E_x}{\nabla_x T} = \frac{E_x}{\nabla_x T} \frac{l_x}{l_x} = \frac{\Delta V_x}{\Delta T_x} = S_{xx}.$$
 (8)

Thus, knowledge of only α_{xx} and σ_{xx} is sufficient to predict the Seebeck effect. The quantity $\frac{\alpha_{xx}}{\sigma_{xx}}$ is known as the Seebeck coefficient $S_{xx} = \frac{E_x}{\nabla_x T}$ (note on sign convention³⁷).

Moving on to the Nernst effect, the off-diagonal terms σ_{xy} and α_{xy} become non-zero when we apply a magnetic field. The magnetic field causes a Lorentz deflection of the thermally generated E_x , and an off-diagonal electrical component $\sigma_{yx}E_x$ is balanced by an off-diagonal thermoelectric (Peltier) component $\alpha_{yx}(-\nabla_x T)$. Now, in addition to J_x , we must consider J_y ,

$$J_{\nu} = \sigma_{\nu x} E_x + \sigma_{\nu \nu} E_{\nu} - \alpha_{\nu x} \nabla_x T = 0. \tag{9}$$

 J_x is no longer equal to the expression in Eq. (7), but off-diagonal terms are now included due to the magnetic field applied,

$$J_x = \sigma_{xx} E_x + \sigma_{xy} E_y - \alpha_{xx} \nabla_x T = 0.$$
 (10)

By plugging in $E_x = \frac{\alpha_{xx}}{\sigma_{xx}} \nabla_x T - \frac{\sigma_{xy}}{\sigma_{xx}} E_y$ in Eq. (10), we produce an expression for the Nernst signal,¹⁰

$$\frac{E_y}{\nabla_x T} = \frac{\alpha_{xy} \sigma_{xx} - \alpha_{xx} \sigma_{xy}}{\sigma_{xx}^2 + \sigma_{xy}^2}.$$
 (11)

By assuming that $\sigma_{xy}^2 \ll \sigma_{xx}^2$ (low magnetic field), we can rearrange Eq. (11),

$$\frac{E_y}{\nabla_x T} = \frac{\alpha_{xy}}{\sigma_{xx}} - \frac{\alpha_{xx}}{\sigma_{xx}^2} \sigma_{xy}.$$
 (12)

Multiplying the first term of Eq. (12) by α_{xx}/α_{xx} leads to the further simplified equation,

$$\frac{E_y}{\nabla_x T} = S_{xx} \left(\frac{\alpha_{xy}}{\alpha_{xx}} - \frac{\sigma_{xy}}{\sigma_{xx}} \right). \tag{13}$$

The Nernst signal $E_y/\nabla_x T$ is sometimes referred to in the literature as S_{yx} or the Nernst thermopower, to distinguish it from the longitudinal thermopower or Seebeck coefficient.¹⁵ It is tempting to draw the conclusion upon inspection of Eq. (13) that a large Seebeck coefficient (S_{xx}) will lead to a large Nernst signal, but in fact, we should draw our attention to the terms in parentheses. The second term in

parentheses in Eq. (13) is σ_{xy}/σ_{xx} ; this term can be related to the Hall angle, θ_H . The magnitude of θ_H can be considered a measure of how strongly a drifting charge carrier is deflected in a transverse magnetic field due to the Lorentz force. The deflection can be viewed as the sum of two orthogonal vectors: $\sigma_{xx}\hat{x} + \sigma_{xy}\hat{y}$. The inner angle therein is thus given by $\sigma_{xy}/\sigma_{xx} \equiv \tan(\theta_H)$. Similarly, the thermally driven carriers deflect in the magnetic field. The first term in parentheses on Eq. (13) is $\alpha_{xy}/\alpha_{xx} \equiv \tan(\theta_\alpha)$. Thus, the Nernst coefficient is a fight between the thermoelectric term $\tan(\theta_\alpha)$ and the Hall term $\tan(\theta_H)$.

Now that we have considered what is measured macroscopically when performing a Nernst measurement, we consider the solutions to the Boltzmann transport equation using the transport distribution function, or TDF. The TDF in the case of periodic crystalline materials is 10,11,36,38

$$\Sigma(E) = g(E)v(E)^2\tau(E), \tag{14}$$

where E is the energy, g(E) is the density of states, v(E) is the group velocity of charge carriers along the direction of transport, and $\tau(E)$ is the electron relaxation time. If many bands or non-parabolic bands contribute to electron transport, then a summation must be performed instead of the simple Eq. (14). 10,38 The transport coefficients are given by solutions to the Boltzmann equation. We note that $\Sigma(E)$ could be a more complicated summation than the simple case of Eq. (14).

The longitudinal electric (σ) and thermoelectric (α) conductivities are given below in terms of the TDF. For brevity, we omit the subscript on longitudinal [on-diagonal components of Eq. (6)] coefficients. For an isotropic compound, $\sigma = \sigma_{xx} = \sigma_{yy} = \sigma_{zz}$,

$$\sigma = e^2 \int_{-\infty}^{\infty} dE \left(\frac{-\partial f_0}{\partial E} \right) \Sigma(E), \tag{15}$$

$$\alpha = e \int_{-\infty}^{\infty} dE \left(\frac{-\partial f_0}{\partial T} \right) \Sigma(E). \tag{16}$$

We can provide Eq. (16) in terms of $\partial f_0/\partial E$ as well

$$\alpha = \frac{e}{T} \int_{-\infty}^{\infty} dE \left(\frac{-\partial f_0}{\partial E} \right) (E - E_F) \Sigma(E). \tag{17}$$

In this form [Eq. (17)], it is even more explicit that the carriers slightly above and below but not exactly at the Fermi contribute to thermoelectric conductivity (α).

The transverse conductivities are as follows: where we pick up a magnetic (perpendicular to the electric field) contribution of μB , where $\mu = e\tau/m_b^*$ (electronic mobility), B is the magnetic field, and m_b^* is the inertial (band) mass (which is equal to the density of state mass in a single band model),

$$\sigma_{\perp} = e^2 \int_{-\infty}^{\infty} dE \left(\frac{-\partial f_0}{\partial E} \right) \Sigma(E) \frac{\mu B}{1 + \mu^2 B^2}. \tag{18}$$

Under low field conditions, $\mu B \ll 1$, and the formula simplifies to

$$\sigma_{\perp} = e^2 \int_{-\infty}^{\infty} dE \left(\frac{-\partial f_0}{\partial E} \right) \Sigma(E) \mu B. \tag{19}$$

Making the same consideration as above for low-field conditions, the transverse thermoelectric conductivity is

$$\alpha_{\perp} = \frac{e}{T} \int_{-\infty}^{\infty} dE \left(\frac{-\partial f_0}{\partial E} \right) (E - E_F) \Sigma(E) \mu B.$$
 (20)

Equations (15)–(20) can be used to write an expression for the Nernst coefficient [Eq. (11)] in terms of the TDF. Similarly, expressions for the electrical conductivity [Eq. (15)] Seebeck coefficient (α/σ) and Hall coefficient ($\sigma_{xy}/B \sigma_{xx}^2$) can be developed. In practice, these expressions are considered under the constraints and boundary conditions of various models, including single or multiband Kane, bipolar, or single or multiband parabolic models. Employing a parabolic or Kane band model is quite common. $^{4.7,24,39}$ In the next section, we focus on the single parabolic band (SPB) model.

The SPB model offers a way to solve for the underlying physical parameters that govern a material's electronic properties. The four fundamental electronic transport parameters (τ, r, E_F, m^*) are visible in Eqs. (21)–(24), although some do not contain all four. Along with the parabolic band approximations, an additional assumption is generally made during analysis. This assumption is that scattering time follows a power law: $\tau = \tau_0 E^{r-0.5}$, where τ is the carrier relaxation time, τ_0 is the relaxation time prefactor, and r is the scattering exponent. The scattering exponent r typically adopts a value between 0 (acoustic phonon scattering) and 2 (ionized impurity scattering). Within the single parabolic band model, the effective mass density of states m_{DOS}^* is equal to the inertial band mass m_b^* , but for degenerate systems, this assumption cannot be made. Under the SPB model, the solution to the Boltzmann equation for the Nernst coefficient yields³

$$N = k_B \frac{\tau_0}{m^*} \left(\frac{(r+1)F_r(\eta)(2r+3/2)F_{2r+1/2}(\eta)}{[(r+1)F_r(\eta)]^2} - \frac{(2r+1/2)F_{2r-1/2}(\eta)(r+2)F_{r+1}(\eta)}{[(r+1)F_r(\eta)]^2} \right), \tag{21}$$

where F_r refers to the Fermi integral: $\int_0^\infty \frac{\varepsilon' d\varepsilon}{1+Exp(\varepsilon-\eta)}$. We provide the equations for Boltzmann solutions to equations for R_H , S, and σ as follows:³

Electric conductivity:

$$\sigma = \frac{e^2 (2k_B T)^{3/2}}{3\pi^2 h^3} m^{*1/2} \tau_0(r+1) F_r(\eta). \tag{22}$$

Seebeck:

$$S = \frac{k_B}{e} \left(\frac{(r+2)F_{r+1}(\eta)}{(r+1)F_r(\eta)} - \eta \right). \tag{23}$$

Hall:

$$R_{H} = \frac{1}{e} \left(\frac{(2r+1/2)F_{2r-1/2}(\eta)}{\left\lceil (r+1)F_{r}(\eta) \right\rceil^{2}} \right) \left(\frac{3\pi^{2}\hbar^{3}}{(2m^{*}k_{B}T)^{3/2}} \right).$$
(24)

Within the SPB and power law scattering approximations, the four material parameters encompassed by the TDF $(m^*, \tau, r,$ and $E_F)$ can be calculated by solving a system of four equations [Eqs. (21)–(24)] with four measurable transport coefficient values as

input. Measuring S, R_H , σ , and N and solving the system of equations is deemed the *method of four coefficients*. ^{3,7,21,40}

The *method of four coefficients* has been employed over the past couple of decades by researchers deeply interested in the material limits to electron mobility across a breadth of fields, including thermoelectrics 4,7,8,24,41 and transparent conducting oxides. 21,40,42 Without measuring Nernst, an assumption about one of the variables is required. This can lead to an inaccurate calculation of the fundamental material parameters. 3,43,44 In practice, the value of r is often assumed to be 0, which can lead to incorrect calculations of the TDF. 43,44 The Nernst effect is incredibly sensitive to scattering type, 3,6,15 and measuring N can lead to more accurate solutions to the TDF.

SUPPLEMENTARY MATERIAL

See the supplementary material for figures on simulated heat flow, magnet calibration, sample geometry optimization, and additional measurements showing slower magnetic field sweep and the error in voltage readings. The data used to generate the figures in the manuscript as well as the supplement are provided in .xlsx format.

ACKNOWLEDGMENTS

The authors thank J. P. Heremans, D. L. Young, and J. B. Martin for their helpful conversations. The research was supported by the National Science Foundation (NSF) Division of Materials Research (CAREER Award No. 1555340). C.E.P. and E.S.T. acknowledge the funding from the NSF Office of Advanced Cyberinfrastructure, Grant No. 2118201. C.M.C. acknowledges the funding from the NASA Science Mission Directorate's Radioisotope Power Systems Thermoelectric Technology Development Project under Grant Nos. NNX16AT18H and 80NSSC19K1290. In addition, the research was carried out at the Jet Propulsion Laboratory, California Institute of Technology, under a contract with the National Aeronautics and Space Administration (Grant No. 80NM0018D0004).

AUTHOR DECLARATIONS

Conflict of Interest

The authors have no conflicts to disclose.

Author Contributions

C. E. Porter: Conceptualization (equal); Data curation (lead); Formal analysis (equal); Investigation (equal); Methodology (lead); Software (lead); Visualization (lead); Writing – original draft (lead); Writing – review & editing (equal). C. M. Crawford: Conceptualization (equal); Software (supporting); Writing – review & editing (equal). E. S. Toberer: Conceptualization (equal); Funding acquisition (lead); Investigation (equal); Methodology (equal); Project administration (equal); Resources (equal); Supervision (lead); Writing – review & editing (equal).

DATA AVAILABILITY

The data that support the findings of this study are available within the article and its supplementary material.

REFERENCES

- ¹K. Behnia, C. R. Phys. 23, 25 (2022).
- ²K. Behnia and H. Aubin, Rep. Prog. Phys. **79**, 046502 (2016).
- ³C. M. Crawford, E. A. Bensen, H. A. Vinton, and E. S. Toberer, Phys. Rev. Appl. 16, 024004 (2021).
- ⁴J. P. Heremans, V. Jovovic, E. S. Toberer, A. Saramat, K. Kurosaki, A. Charoenphakdee, S. Yamanaka, and G. J. Snyder, Science 321, 554 (2008).
- ⁵Y. Wang, Z. A. Xu, T. Kakeshita, S. Uchida, S. Ono, Y. Ando, and N. P. Ong, Phys. Rev. B **64**, 224519 (2001).
- ⁶D. L. Young, T. J. Coutts, and V. I. Kaydanov, Rev. Sci. Instrum. 71, 462 (2000).
- ⁷ J. P. Heremans, C. M. Thrush, and D. T. Morelli, Phys. Rev. B 70, 115334 (2004).
 ⁸ T. Arisaka, M. Otsuka, and Y. Hasegawa, J. Appl. Phys. 123, 235107 (2018).
- ⁹M. K. Zhitinskaya, S. A. Nemov, and L. D. Ivanova, Phys. Solid State 44, 42 (2002).
- 10 K. Behnia, $Fundamentals\ of\ Thermoelectricity\ (Oxford\ University\ Press,\ Oxford,\ 2015).$
- ¹¹ A. Zevalkink, D. M. Smiadak, J. L. Blackburn, A. J. Ferguson, M. L. Chabinyc, O. Delaire, J. Wang, K. Kovnir, J. Martin, L. T. Schelhas, T. D. Sparks, S. D. Kang, M. T. Dylla, G. J. Snyder, B. R. Ortiz, and E. S. Toberer, Appl. Phys. Rev. 5, 021303 (2018).
- ¹² Note the difference in units between Nernst signal $(E_y/\nabla_x T)$: $\mu V/K$ vs Nernst coefficient $E_y/(\nabla_x TB_z)$): $\mu V/KT$.
- ¹³E. H. Putley, *The Hall Effect and Semi-Conductor Physics* (Dover Publications, New York, 1968).
- ¹⁴J. C. G. de Sande and J. M. Guerra, Phys. Rev. B 45, 11469 (1992).
- ¹⁵ M. Murata, K. Nagase, K. Aoyama, and A. Yamamoto, Appl. Phys. Lett. 117, 103903 (2020).
- ¹⁶K. Behnia, J. Phys.: Condens. Matter **21**, 113101 (2009).
- ¹⁷X. Zhou, H. Liu, W. Wu, K. Jiang, Y. Shi, Z. Li, Y. Sui, J. Hu, and J. Luo, Phys. Rev. B **105**, 205104 (2022).
- ¹⁸Y. Yang, Q. Tao, Y. Fang, G. Tang, C. Yao, X. Yan, C. Jiang, X. Xu, F. Huang, W. Ding, Y. Wang, Z. Mao, H. Xing, and Z.-A. Xu, Nat. Phys. 19, 379 (2023).
- ¹⁹H. Jin and J. P. Heremans, Phys. Rev. Mater. **2**, 115401 (2018).
- ²⁰ I. P. Molodyan, D. N. Nasledov, S. I. Radautsan, and V. G. Sidorov, Phys. Status Solidi B 18, 677 (1966).
- ²¹ V. Kaydanov, T. J. Coutts, and D. L. Young, "Studies of band structure and free carrier scattering in transparent conducting oxides based on combined measurements of electron transport phenomena," Tech. Rep., National Renewable Energy Lab.(NREL), Golden, CO, USA, 2000.
- ²²S. Sharma and C. S. Yadav, Rev. Sci. Instrum. **91**, 123907 (2020).
- 23 T. Arisaka, M. Otsuka, M. Tokitani, and Y. Hasegawa, J. Appl. Phys. 126, 085101 (2019).
- ²⁴ V. Jovovic, S. J. Thiagarajan, J. P. Heremans, T. Komissarova, D. Khokhlov, and A. Nicorici, J. Appl. Phys. **103**, 053710 (2008).
- ²⁵ M. Parzer, T. Schmid, F. Garmroudi, A. Riss, T. Mori, and E. Bauer, Rev. Sci. Instrum. **95**, 043906 (2024).
- ²⁶ K. A. Borup, E. S. Toberer, L. D. Zoltan, G. Nakatsukasa, M. Errico, J.-P. Fleurial, B. B. Iversen, and G. J. Snyder, Rev. Sci. Instrum. 83, 123902 (2012).
- ²⁷J. Martin, T. Tritt, and C. Uher, J. Appl. Phys. **108**, 121101 (2010).
- ²⁸S. Iwanaga, E. S. Toberer, A. LaLonde, and G. J. Snyder, Rev. Sci. Instrum. **82**, 063905 (2011).
- ²⁹Y. Wu, S. Dutta, J. Jesudasan, A. Frydman, and A. Roy, Rev. Sci. Instrum. 91, 095112 (2020).
- ³⁰ M. R. Scudder, K. G. Koster, J. P. Heremans, and J. E. Goldberger, Appl. Phys. Rev. 9, 021420 (2022).
- ³¹ J. Martin, Meas. Sci. Technol. **24**, 085601 (2013).
- ³²F. Werner, J. Appl. Phys. **122**, 135306 (2017).

- ³³ Y. Jia, J. Liu, A. Matsushita, M. Lan, P. Klavins, and R. Shelton, Phys. Rev. B 46, 11745 (1992).
- ³⁴ X. Mi, W. Xia, L. Zhang, Y. Gan, K. Yang, A. Wang, Y. Chai, Y. Guo, X. Zhou, and M. He, New J. Phys. 24, 093021 (2022).
- ³⁵T. C. Harman and J. M. Honig, *Thermoelectric and Thermomagnetic Effects and Applications* (McGraw-Hill, Inc., New York, 1967).
- ³⁶Electron Transport in Compound Semiconductors, Springer Series in Solid-State Sciences, edited by B. Nag, M. Cardona, P. Fulde, and H.-J. Queisser (Springer, Berlin, Heidelberg, 1980), Vol. 11.
- 37 Sometimes in the literature there is a negative before the temperature gradient. This reflects choice of convention, but at the end of the day a positive Seebeck coefficient generally represents p-type semiconductors.
- ³⁸G. Mahan and J. Sofo, Proc. Natl. Acad. Sci. U. S. A. **93**, 7436 (1996).
- ³⁹ J. P. Heremans, C. M. Thrush, and D. T. Morelli, J. Appl. Phys. **98**, 063703 (2005).
- ⁴⁰T. J. Coutts, D. L. Young, X. Li, W. Mulligan, and X. Wu, J. Vac. Sci. Technol. A **18**, 2646 (2000).
- ⁴¹Y. Kajikawa, J. Appl. Phys. **119**, 055702 (2016).
- 42 D. L. Young, H. Moutinho, Y. Yan, and T. J. Coutts, J. Appl. Phys. 92, 310 (2002).
- ⁴³ A. M. Ganose, J. Park, A. Faghaninia, R. Woods-Robinson, K. A. Persson, and A. Jain, Nat. Commun. **12**, 2222 (2021).
- ⁴⁴ A. M. Ganose, J. Park, and A. Jain, "The temperature-dependence of carrier mobility is not a reliable indicator of the dominant scattering mechanism," arXiv:2210.01746 [cond-mat.mtrl-sci] (2022).